Journal of Colloid and Interface Science 576 (2020) 195–202

Contents lists available at ScienceDirect

Journal of Colloid and Interface Science

journal homepage: www.elsevier.com/locate/jcis

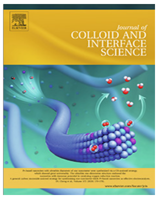

In situ investigation of particle clustering dynamics in colloidal assemblies using fluorescence microscopy

Youngjoon Suh[a], Hamsa Gowda[b], Yoonjin Won[a,*]

[a] Department of Mechanical and Aerospace Engineering, University of California, Irvine 5200 Engineering Hall, CA 92617-2700, USA
[b] Department of Biomedical Engineering, University of California, Irvine 3120 Natural Sciences II, CA 92697-2715, USA

GRAPHICAL ABSTRACT

Herein, particle clustering dynamics and thermofluidic transprot in colloidal assemblies are experimentally examined using a novel fluorescence technique with the aim to investigate colloidal physics that decide cracking mechanics during self-assembly. The results show that grain boundaries are determined by dynamic structuring regimes governed by the film's saturation level.

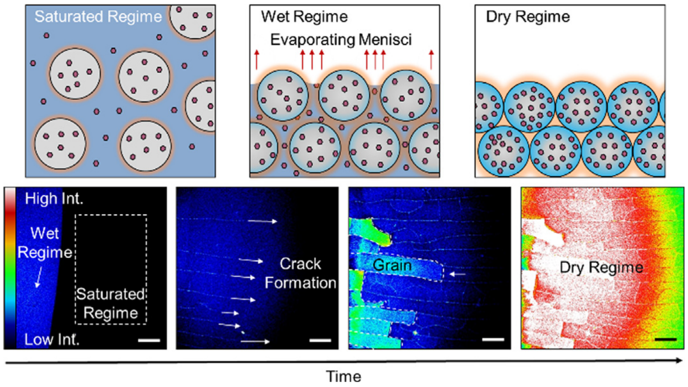

ARTICLE INFO

Article history:
Received 21 February 2020
Revised 4 April 2020
Accepted 11 April 2020
Available online 17 April 2020

Keywords:
Self-assembly
Saturation level
In situ measurements
Grain boundary
Laser induced fluorescence

ABSTRACT

Colloidal self-assembly is a process in which dispersed matter spontaneously form higher-order structures without external intervention. During self-assembly, packed particles are subject to solvent-evaporation induced dynamic structuring phases, which leads to microscale defects called the grain boundaries. While it is imperative to precisely control detailed grain boundaries to fabricate well-defined self-assembled crystals, the understanding of the colloidal physics that govern grain boundaries remains a challenge due to limited resolutions of current visualization approaches. In this work, we experimentally report *in situ* particle clustering dynamics during evaporative colloidal assembly by studying a novel microscale laser induced fluorescence technique. The fluorescence microscopy measures the saturation levels with high fidelity to identify distinct colloidal structuring regimes during self-assembly as well as cracking mechanics. The techniques discussed in this work not only enables unprecedented levels of colloidal self-assembly analysis but also have potential to be used for various sensing applications with microscopic resolutions.

---

* Corresponding author.
E-mail address: won@uci.edu (Y. Won).

https://doi.org/10.1016/j.jcis.2020.04.054
0021-9797/

1. Introduction

Self-assembly is a process by which matters form into structures through vigorous interparticle interactions and multiscale thermofluidic physics. Among various self-assembly methods, evaporative colloidal self-assembly (Fig. 1a,b) continuously attracts researchers for its simplicity and potential to be scaled up [1–7]. In this method, monodisperse nanospheres assemble themselves into thermodynamically dictated structural organizations, called the colloidal crystals or opals. Previous literatures show the potential use of colloidal crystals in various applications ranging from tunable wavelengths for optics [8–11], fluid transport for electronic cooling devices [12–16], and rigid support for biomimetic tissue scaffolds [17–20]. Most applications require rigorous structural periodicity at the large-scale (>1 cm)[21] in order to ensure isotropic diffraction [9], well-distributed liquid transport [13], and idealistic mechanical environments for cell growth, respectively [20]. However, mishaps in the self-assembly process cause the structures to naturally form microcracks (i.e., grain boundaries) that propagate between packed colloidal crystal domains [22–27].

Cumulative literature over the past decade indicates that the perspective of grain boundaries has been changed. In the past, grain boundaries were considered as "microscale defects." Several efforts to minimize defects have been attempted by increasing the colloidal kinetic energy (i.e., increasing evaporation temperature) [23,24], by decreasing the structural thickness [28–31], by ensuring sufficient self-assembly time [24], or by counteracting sphere shrinkage through sol-gel precursors [32,33]. Despite all efforts pursuing perfect crystal packing, it has been a great challenge to entirely eliminate grain boundaries at the large-scale [34,35]. On the other hand, recent studies have started considering grain boundaries as micro/nanopatterns that can be utilized to design unique optical and liquid transport properties [13,34–39]. Such an alternative approach requires the precise control of volatile cracking phenomena during self-assembly which, in turn, consists of complex intermolecular physics in relation to microscale thermofluidic phenomena.

Early theoretical models have explored the cracking phenomena associated with structural thickness, film stress level, and grain boundary initiation [28,29]. The relationship suggests a "critical thickness" that is required for a colloidal film to release its stress in forms of grain boundaries [28,29]. In addition, grain boundaries also arise from the combination of particle-level defects (i.e., colloidal polydispersity, impurities, and particle shapes) [22] and local packing mismatches (i.e., body-centered cubic (BCC), face-centered cubic (FCC), and hexagonal close-packed (HCP)) [25,40,41]. Despite the previous efforts, a holistic view about cracking phenomena accounting for thermofluidic boundary conditions has not yet been fully explained.

Recent discoveries on colloidal self-assembly suggest that grain boundaries are deeply related to saturation levels. For example, a study reported a drying-induced dynamic local packing transformation from FCC to BCC during nanosphere self-assembly [42,43]. Based on past research, such local packing changes can modify the entropic state of the system and trigger grain boundaries [44]. Furthermore, our past work has demonstrated the control of grain boundaries by modulating evaporation conditions such as surface temperatures [34]. The findings mentioned above suggest that grain boundaries are byproducts of drying-induced transitional states where dynamic interparticle tension forces activate structural changes [40,41,45,46]. Therefore, it is imperative to find a strong correlation between grain boundaries and film saturation levels; however, direct experimental measurements have been challenging due to the limited spatial resolutions of current measurement approach, which motivates us to study new

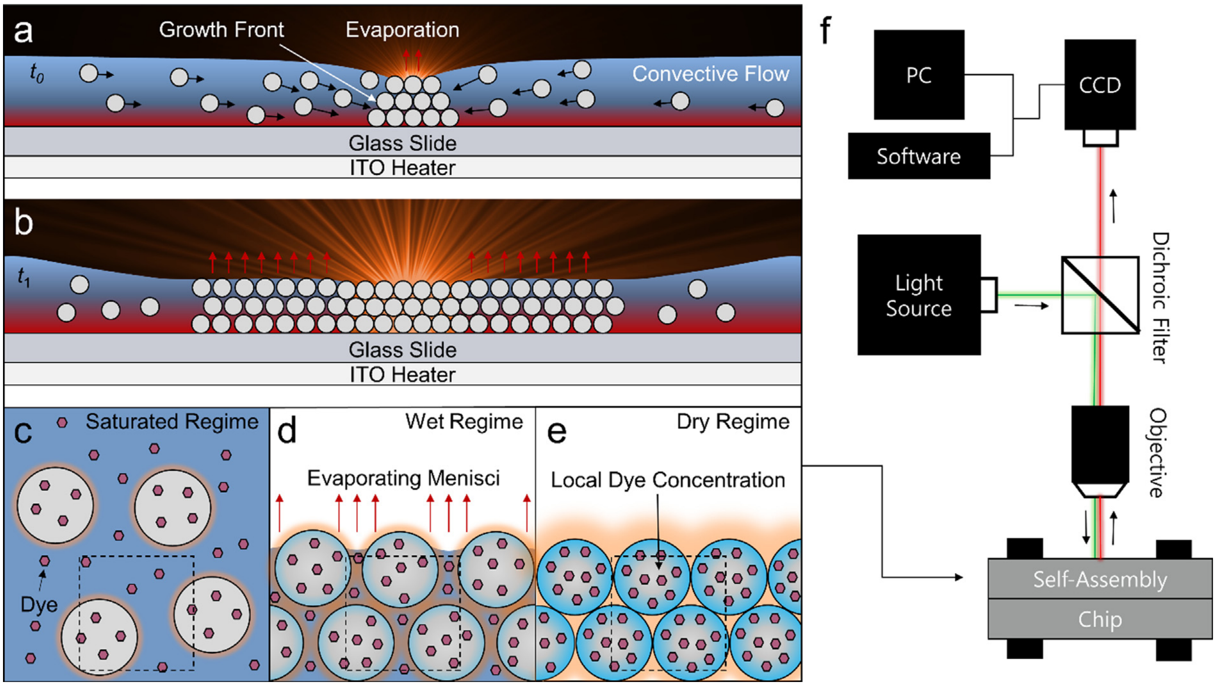

Fig. 1. In situ monitoring of evaporative colloidal self-assembly using microscale laser induced fluorescence (μLIF) techniques. (a) Particles are guided towards a growth front by evaporation-induced convective flows. An ordered structure of colloidal spheres forms as more spheres accumulate. t_o and t_1 represent different time frames. (b) As nanospheres start to assemble into crystalline opals, a relatively constant thickness film develops. (c–e) The number of dye particles loaded onto colloidal particles and mean distances between doped particles dictates the saturation level of the film and thereby the fluorescence intensity. The figures illustrate how the local dye concentration changes during the three distinctive regimes called the (c) saturated regime, the (d) wet regime, and the (e) dry regime. The change in fluorescence intensity is illustrated as orange luminance. (f) During the μLIF measurement, a light source (green) excites the dye particles, causing it to fluoresce light at a higher wavelength. The light passes through an optical filter to a charge-coupled device (CCD) camera and is postprocessed in PC with software.

high-resolution visualization techniques that can identify saturation levels during self-assembly.

Laser induced fluorescence (LIF) techniques can be a powerful methodology to measure thermofluidic properties. LIF techniques utilize fluorescence where light-sensitive particles (i.e., fluorophores) absorb photons of a specific wavelength (i.e., excitation) and then emit photons of longer wavelength (i.e., emission). The emitted signals are transmitted through optical filters to produce fluorescence intensity-based imaging. At the macroscale, LIF techniques have been conventionally used to analyze thermofluidic physics such as temperature fields in a turbulent duct flow [47], droplet impinging dynamics [48], and surface thermal profiles of liquid droplets [49]. Micro laser induced fluorescence (μLIF) employs microscopes to enhance characterization resolutions up to 100–400 nm with high fidelity [50–58,67]. μLIF techniques have successfully demonstrated high-resolution surface temperature measurements in microchannels [55], droplet interfaces [49], and microfabricated devices by using temperature-sensitive fluorescence dyes [59]. However, there have been no efforts to identify the saturation levels under colloidal self-assembly using μLIF techniques due to the complications involved with having additional nanospheres in the fluorescent solutions [60–62]. Despite such complexity, μLIF techniques are suggested to measure saturation levels and explore uncharted thermofluidic colloidal self-assembly physics by exploiting the unique fluorescence behaviors of colloidal and dye mixtures in detail in this paper.

Herein, we study fluorescence microscopy techniques for the first time to experimentally characterize real-time colloid physics during evaporative self-assembly at the submicron scale. The fluorescence microscopy techniques are suggested to identify distinct structuring regimes dictated by their saturation levels. High-resolution measurements will allow us to examine the detailed particle clustering dynamics and thermofluidic transport during evaporative self-assembly, resulting in the formation of grain boundaries or microcracks between crystal opals and their propagation. The crack formation and propagation physics reported in this work are valuable for studies aiming to fabricate crystalline structures with well-defined features and transport properties. Furthermore, the techniques provided in this work have potential to serve as advanced environmental sensing tools for biomedical, microfluidic, and electronic applications.

2. Results and discussion

In evaporative colloidal self-assembly, dispersed nanospheres assemble themselves to form structures as follows: As the solvent evaporates, colloidal nanospheres start adhering to the substrate near the meniscus line, forming small organizations of packed spheres, which is denoted as the growth front (Fig. 1a). Nearby nanospheres are driven towards the growth front via capillary-induced water flows, leading to a highly ordered, crystalline thin film (Fig. 1b). Despite the crystallinity at the large scale, microscale structural defects (i.e., grain boundaries) naturally form and propagate throughout the film. In order to understand the colloidal physics that generate grain boundaries, we explore the impact of saturation levels on the transition from dispersed nanospheres to highly ordered, crystalline thin films by using μLIF techniques (Fig. 1f). The μLIF techniques enable real-time observation of saturation levels by tracking the fluorescence intensity of the mixture of rhodamine B and polystyrene latex beads (hereafter denoted as RhB@PLB).

The evaporation phenomena during the self-assembly process impact the overall RhB@PLB's fluorescence intensity in relation to the combination of the medium thickness and the number of fluorophores per unit volume (i.e., local dye concentration). The dynamic medium thickness influences the fluorescence intensity by dictating the dye-incorporated media volume the excitation light passes through [63], which means the fluorescence intensity decreases with smaller medium thickness. The initial solution state has excess solvent with respect to spheres and the overall fluorescence intensity is thereby mainly dominated by the evaporation. It should be noted that the medium thickness becomes relatively constant if the solvent level is below the film thickness of packed nanospheres. (Fig. 1b). In addition, the number of fluorophore particles loaded onto nanospheres increases (Fig. S1a–c), and the mean distance between doped particles decreases, as the solvent evaporates. This all consequentially increases the local dye concentration and fluorescence intensity, as illustrated in Fig. 1c–e. Since the medium thickness effect is negligible when the nanospheres begin to assemble into films, we hypothesize that the fluorescence intensity is mainly governed by the solvent saturation levels in this study. A constant sphere size and colloidal concentration of 300 nm and 4%, respectively, is selected (See Supporting Information S1).

To validate the hypothesis described above, we characterize the real-time self-assembly process by identifying different regimes – (1) the saturated regime, (2) the wet regime, and (3) the dry regime (Fig. 2). The saturated regime (Fig. 2a) describes the state before nanosphere structuring. The excess solvent in the saturated regime allows both dye and nanosphere particles to move throughout the solution with relatively long interparticle distances that result in weak fluorescence signals (Fig. 2e). As the solvent evaporates, the nanospheres organize themselves into a loosely packed configuration, called the wet regime (Fig. 2b,c). The fluorescence intensity-based image in Fig. 2a shows the wet regime expanding through the saturated regime where the fluorescence intensity increases by approximately 44% (Fig. 2e). The quick transition (~15 s) from the saturated regime to the wet regime indicates rapid nanosphere assembly. The wet regime remains at a relatively constant intensity for 832 s, suggesting that the overall structure's saturation level is preserved during this process. The constant saturation level can be explained by a continuous water flow via capillary wicking from the bulk solution to the growth front. It should be mentioned that minor photobleaching (2−9%) occurs during the wet regime as the film is exposed to the laser for a relatively long time. The bar graph shown in Fig. 2e inset shows the temporal average fluorescence intensity measured from the saturated (0–45 s), wet (70–890 s), and dry (1150–1184 s) regime. The standard deviation of each measurement is calculated as 0.8, 13.1, and 1.2 for saturated, wet, and dry regime, respectively, and is represented by error bars. Finally, the solvent completely evaporates, which stops further liquid delivery, leading to the dry-out domains in the dry regime (Fig. 2d). The transition from the wet to the dry regime is easily identified by an increase in the fluorescence intensity by ~153%, as shown in Fig. 2e.

2.1. Fundamental investigation of longitudinal cracking mechanism

While the overall saturation level measurements reveal the transition between the different regimes during colloidal self-assembly, it is critical to identify local saturation levels to understand cracking phenomena with a high spatial resolution (Fig. 3). The longitudinal cracks first develop in the drying direction (Fig. 2b), followed by the formation of the transverse cracks in later steps.

Movie S2 shows the full self-assembly process while Movie S3 displays the sequential crack propagation steps in detail. First, longitudinal cracks develop in the wet regime where the active assembly of nanospheres starts forming packed structures; as the wet regime expands, the cracks propagate further by tensile stresses accumulated within the film. The propagation of a single longitudi-

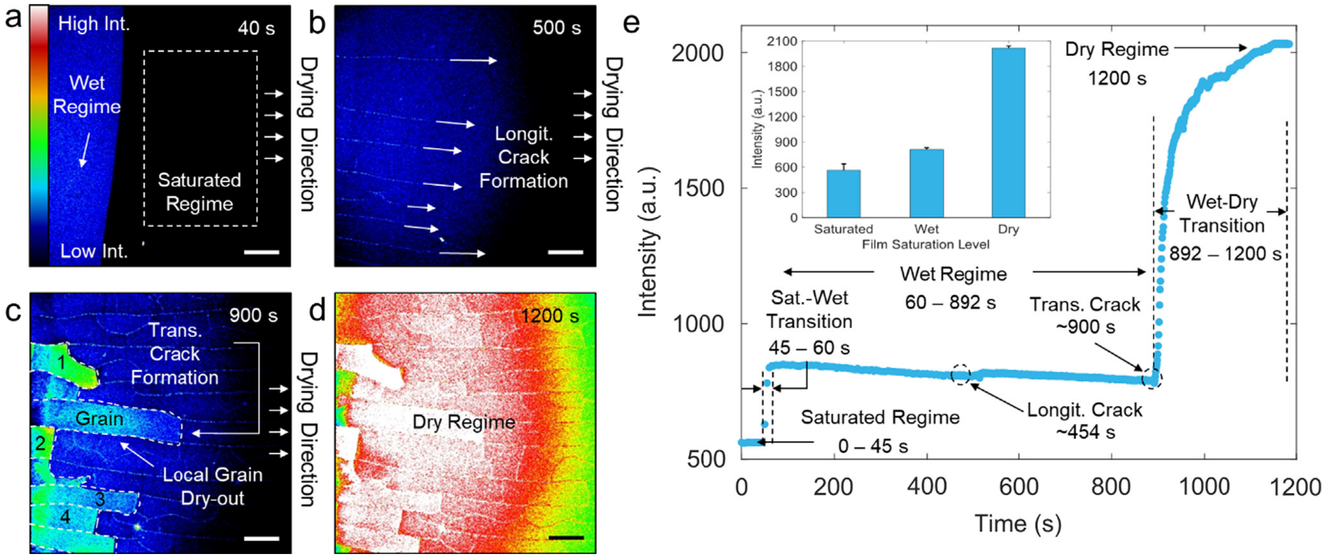

Fig. 2. Distinctive saturation regimes during evaporative self-assembly. (a) The image shows the wet regime expanding through the saturated regime. (b) As the wet regime expands, cracks initiate and propagate in the drying direction (i.e., longitudinal cracks), which are indicated by arrows. (c) At a later stage, cracks perpendicular to the drying direction (i.e., transverse cracks) form and create an isolated domain (i.e., grain). The opal film dries in discrete steps as local grain dry-out occurs. Individual grains are identified with numbers for the dry-out analysis in Fig. 4. (d) The fluorescence intensity abruptly increases after the complete dry-out. The scale bars represent 100 µm. (e) The spatial average fluorescence intensity of the dashed box in (a) shows stepwise increases with time. Each step represents a different saturation regime (e.g., saturated regime, wet regime, and dry regime). The inset shows the temporal average intensity of the dashed box in (a) for each saturation regime.

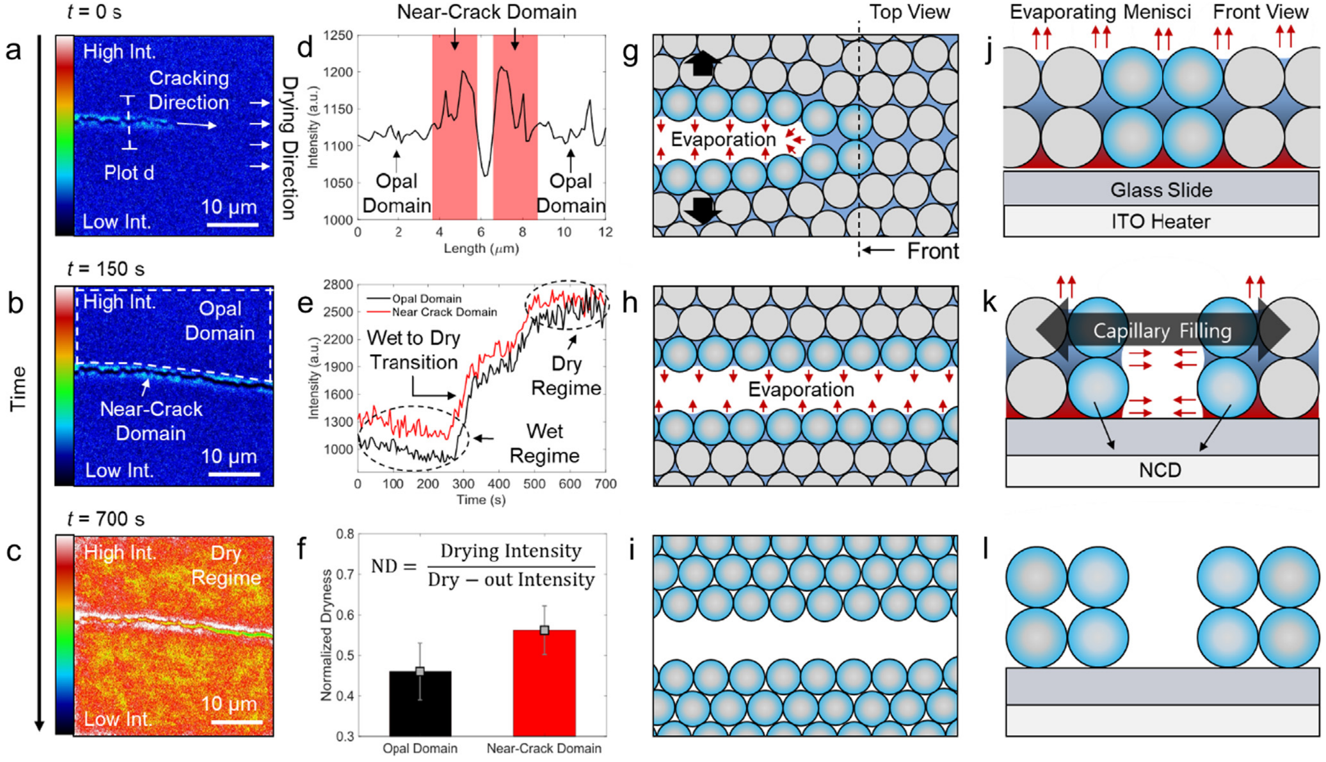

Fig. 3. Crack formation and propagation phenomena associated with the local evaporation. (a–c) High magnified fluorescence images show a longitudinal crack propagating through the film. (a) The drying direction and cracking direction are shown. (b) The opal domain and the near-crack domain is indicated in the figure. (c) Dry-out causes the fluorescence intensity to drastically increase. (d) The fluorescence intensity profile of the dashed line drawn in (a) exhibits high intensities at the near-crack domain (red block). The abrupt dip in fluorescence intensity is caused by the absence of solution at the fissure caused by the crack. (e) Time-dependent plots of the opal and the near-crack domains show fluorescence intensity differences between the two domains decreases as the film dries. (f) The normalized dryness of 5 individual cracks shows that the near-crack domain has a ~22% higher fluorescence intensity than the opal domain during the wet regime, which indicates a lower saturation level. The error bar represents the standard deviation. The crack formation and propagation associated with local evaporation phenomena are illustrated from the (g–i) top and (j–l) front view. The blue and grey color represent dry and wet nanospheres, respectively.

nal crack through the film as well as the differences in local saturation levels are confirmed by time-dependent, high-magnification μLIF images in Fig. 3a–c. The crack peripherals (denoted as the near-crack domain) emit higher fluorescence intensity when compared to the rest of the bulk film (denoted as the opal domain), as plotted in Fig. 3d. Furthermore, the black and red lines in Fig. 3e show the average fluorescence intensity of opal and near-crack domain, respectively, as the regime transforms from the wet to the dry regime. The temporal average fluorescence intensity is taken over the dotted box in Fig. 3b and over a line along the crack peripheral for the opal and near-crack domain, respectively. In the wet regime, the difference in average fluorescence intensity between the opal domain and the near-crack domain remains relatively constant. However, the difference in the average fluorescence intensity gradually diminishes as the film dries. This means that the near-crack domain is drier than the opal domain during the wet regime. The temporal fluorescence intensity fluctuation in Fig. 3e is attributed to background and Poisson noise associated with high-resolution imaging [64–66], where a maximum standard deviation of 91 is reported for the opal domain in the dry regime.

The saturation level difference between the opal domain and the near-crack domain can be explained by the capillary-assisted evaporation after grain boundary formation. Fig. 3g–l illustrates the front and top view cracking schematics, where the blue and grey spheres represent dry and wet nanospheres, respectively. Before cracks are introduced to the film, the evaporating menisci is primarily located at the top of the sphere array, as shown in Fig. 3j. As longitudinal cracks steadily propagate through the film and generate gaps between the packed spheres (Fig. 3g and h), water flux comes from the crack area to the organized spheres through the capillary-assisted wicking and creates additional evaporative surfaces, as illustrated in Fig. 3k. Therefore, capillary-assisted evaporation occurs at the near-crack and causes the near-crack domain to dry faster (Fig. 3h and k). Eventually the opal film consisting of packed spheres completely dries, as illustrated in Fig. 3i and l.

The differences in the saturation levels between the opal domain and the near-crack domain in the wet regime are identified by defining a "normalized dryness (ND)," which is the ratio of fluorescence intensity to the average fluorescence intensity of the dry regime. The ND of the near-crack domain (ND = 0.5) is approximately 22% higher than that of the opal domain (ND = 0.4) where the dry regime ND = 1. This result quantitatively indicates that the near-crack domain is drier than the opal domain.

The results suggest that evaporation rate misbalances between the opal domain and the near-crack domain expediate the longitudinal crack propagation. The evaporation rate misbalances between the opal domain and the near-crack domain can generate auxiliary drying-induced tension forces in the transverse direction, which would encourage longitudinal cracking (Fig. 4a). The tendency for longitudinal cracks to propagate prominently in evaporative colloidal self-assembly is in coherence with our past report where longitudinal crack initiation cites appeared foremost due to the effect of the drying direction [34]. In other words, favorable initiative cites and local evaporation rate misbalances induces a systematic, selective promotion of longitudinal cracking.

2.2. Transverse crack formation and local grain dry-out

Transverse cracks – the cracks that develop normal to the drying direction - form due to force misbalances within the film, which is similar to longitudinal cracks. However, unlike longitudinal cracks (Fig. 4a), transverse cracks consume less time to fully develop due to their short lengths and usually develop at a later stage (Fig. 4b). A set of both longitudinal and transverse cracks creates an isolated opal domain, called the crystal grain or the grain (Fig. S3a). With this in mind, the drying process of the overall film can be considered as a comprehensive drying of individual grains over time (i.e., local grain dry-out).

μLIF observations reveal that individual grains dry in a systematic, step-by-step procedure driven by microscopic liquid transport phenomena. Fig. 4c represents *in situ* saturation levels of individual grains numbered in Fig. 2c. The measurement starts when the first longitudinal cracks appear in the visualization window at t = 454 s and ends when the film fully dries at t = 1200 s. The multiple stepwise fluorescence intensity jumping in Fig. 4c indicate asynchronous drying in local film areas (i.e., grains). The intensity discrepancies of individual grains upon dry-out (~t = ~1200 s) in Fig. 4c are attributed to grain lift-off effects, explained in Supporting Information S2, Fig. S3. Interestingly, the fluorescence intensity in Fig. 4c jumps immediately after the formation of transverse cracks while remaining unchanged during the longitudinal crack's earlier development. This phenomena can be explained by selective capillary-assisted liquid transport from the bulk liquid to the grains. As noted in previous sections, the presence of the nanoscale pores between packed spheres enables liquid feeding from the bulk solution to the growth front via capillary wicking. However, grain boundaries work as hydraulic resistances as the liquid in the created grain boundaries is quickly absorbed by the surrounding opal structures (Fig. 3k). Therefore, grain boundaries can create innately different liquid transport impediments depending on their propagation direction. On the one hand, the longitudinal cracks have minimum impact on liquid transport because they

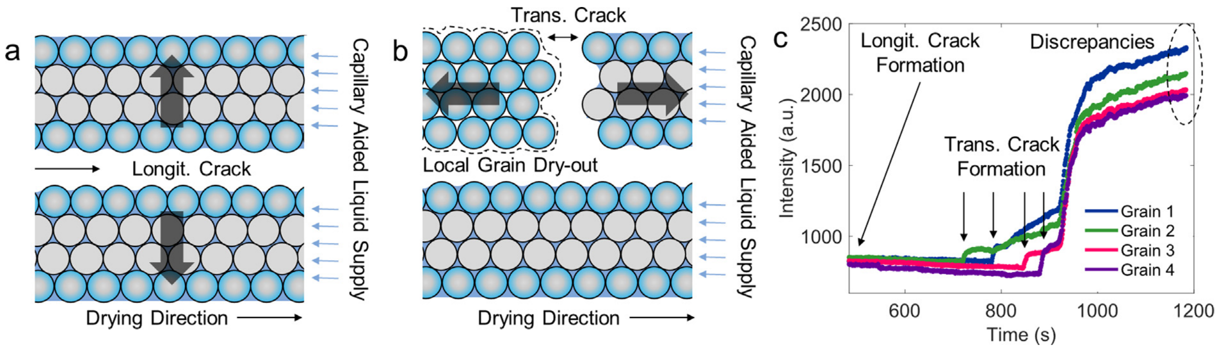

Fig. 4. Grain dry-out mechanism. (a) As longitudinal cracks form, the separated structures are continuously supplied with liquid via capillary wicking. Longitudinal cracks form due to tensile forces (indicated in black arrows) in the direction perpendicular to the drying direction. On the other hand, (b) transverse cracks form due to tensile forces parallel to the drying direction (indicated in black arrows). Transverse cracks prevent further liquid supply to the isolated structure (i.e., grain), which leads to local grain dry-out. (c) The average intensity of individual grains in Fig. 2c displays a stepwise increase right after transverse cracks form. The arrows indicate when longitudinal and transverse cracks start to form.

are in alignment with the direction of the liquid supply (Fig. 4a). On the other hand, the transverse crack creates a gap in a direction that impedes capillary feeding (Fig. 4b). The hydraulic resistances along the liquid feeding originated from the transverse cracks facilitate local grain dry-outs, which results in non-simultaneous film dry-out.

3. Conclusion

In summary, we employ for the first time a μLIF technique that overcomes extant resolution barriers to experimentally characterizes real-time particle clustering dynamics in colloidal assemblies that decide grain boundary formation mechanisms with up to 300 nm spatial resolution. Our method identifies three distinctive saturation level-dictated structuring phases called the saturated, the wet, and the dry regime. The fluorescence intensity increases by 44% and 153% during saturated to wet regime and wet to dry regime transition, respectively. The saturation level jumps indicate discrete saturation level reductions during the self-assembly process. The quick transition (~15 s) from saturated to wet regime suggest a rapid structuring of nanospheres. In addition, grain boundaries form in the wet regime where the local saturation level measurements show that the near-crack domain has 22% lower normalized dryness than the opal domain, suggesting the existence of microscale evaporation rate misbalances between the two domains. The evaporation rate misbalances in turn can cause auxiliary tensile forces that especially promote longitudinal cracks. Furthermore, *in situ* saturation level monitoring shows that transverse cracks function as hydraulic barriers that trigger local grain dry-out, which eventuate in non-simultaneous film dry-out. The findings in this study provide fundamental groundworks for developing a practical approach (e.g., harnessing grain boundaries to fabricate controlled microstructures) to tackle problems engendered by inevitable defects developed in self-assembled structures at the large scale (>1 cm) [34,35,38].

The μLIF technique presented in this study also shows potential to be developed for advanced sensing technology. For example, our μLIF techniques demonstrate high sensitivity (Fig. S1) and reversibility (Fig. S2), which might be useful to detect unintentional local dry-out locations in microfluidic channels. In addition, the techniques might have potential to be exploited as *in situ* stress measurement tools. As future work, we will investigate the correlation between interparticle saturation levels and particle distances to derive quantitative measurements for drying-induced tensile stresses in thin films.

4. Experimental section

4.1. RhB@PLB solution

We fabricate colloidal solutions by incorporating fluorescent dyes into polystyrene latex beads, in order to measure the level of saturation as a function of fluorescence intensity. Prior to the addition of rhodamine B (Acros Organics), a 0.1 M sodium bicarbonate buffer at pH 9.4 is prepared to ensure proper color concentration of the dye. The buffer is made with 30 ml of 0.1 M sodium carbonate and 70 ml of 0.1 M sodium bicarbonate and is diluted to 0.2 mM. Then, rhodamine B is added to the buffer solution to make a 0.1 mM fluorescence solution. The rhodamine B solutions are refined before use with a syringe filter (0.2 μm pore size). After this, monodisperse sulfate latex beads with an 8% concentration (Thermofisher Scientific, Life Technologies Corporation) and particles with 300 nm diameter are dispersed in diluted water via sonication for 20 min. Finally, the colloidal solution is diluted from 8% to 4% by adding rhodamine B solutions to create the RhB@PLB solution.

4.2. Fabrication of crystalline opal Structures.

Crystalline opal structures are fabricated by drop-casting 200 μl of 4% RhB@PLB on the glass substrate of a custom self-assembly chip. The volume and concentration of the solution is determined through a parametric study to produce preferable structural features optimal for imaging during the evaporative deposition (Supporting Information S3, Fig. S4). After the solution is drop-casted, the solution is manually distributed (Fig. S5) using a pipette tip until the solution peripherals are in contact with the side walls of the self-assembly chamber. The indium-tin-oxide (ITO) heater on the glass substrate is heated up at a constant heat flux of 0.75 W/cm^2 by connecting with a power supply. The heated glass substrate enables the drop-casted solution to start forming into thin films as illustrated in Fig. 1a and b.

4.3. Custom self-assembly chip

We design a customized chip to visualize the colloidal self-assembly by using an upright microscope (Fig. S6). The chip consists of top and bottom acrylic platforms, a removable glass slide, a rubber gasket, spring-loaded pogo pins, and a transparent ITO heater (Fig. S6a). The top and bottom substrates are machined using computer numerical control (CNC) machine to ensure the liquid feeding without leakage. Top and side views of the chip are shown in Fig. S6b and c.

4.4. Image acquisition

Fluorescence imaging of the rhodamine dye is performed using an upright confocal fluorescence microscope (BX61, Olympus) with a 10 mm long working distance objective. The upright microscope enables top to bottom surface imaging and thus is suitable for surface analysis. An appropriate filter set (excitation: band pass 559 nm, emission: band pass 570–800 nm) and a broadband mercury illumination are used. For saturation level measurements, a low lasing intensity of 0.3% (to reduce photobleaching of the fluorophore) excites the fluid at wavelengths of 559 nm to fluoresce while the fluorimeter records the fluorescence spectra. The high voltage (HV) and gain are set manually and are kept constant throughout a given set of experiments. Digital images are obtained and post-processed through FluoView FV1000 software. Image colors are added using built-in channel options.

CRediT authorship contribution statement

Youngjoon Suh: Conceptualization, Methodology, Investigation, Writing - original draft, Visualization, Formal analysis. **Hamsa Gowda:** Resources, Methodology. **Yoonjin Won:** Supervision, Writing - review & editing.

Declaration of Competing Interest

The authors declare that they have no known competing financial interests or personal relationships that could have appeared to influence the work reported in this paper.

Acknowledgements

The work was sponsored by the National Science Foundation (NSF), (CBET-TTP 1752147, Thermal Transport Processes). The authors acknowledge the valuable support from the Laboratory for Fluorescence Dynamics and Optical Biology Core, where the fluorescence characterization was performed. Special thanks to Dr. Adeela Syed for her technical support on confocal microscopy technology. Y.S. is thankful for the financial support from the UC Irvine Mechanical and Aerospace Engineering Department Graduate Fellowship.

Appendix A. Supplementary data

Supplementary data to this article can be found online at https://doi.org/10.1016/j.jcis.2020.04.054.

References

[1] M. Holgado, F. Garcia-Santamaria, A. Blanco, M. Ibisate, A. Cintas, H. Miguez, C. Serna, C. Molpeceres, J. Requena, A.J.L. Mifsud, Electrophoretic deposition to control artificial opal growth, Langmuir 15 (14) (1999) 4701–4704.

[2] P. Jiang, M.J. McFarland, Large-scale fabrication of wafer-size colloidal crystals, macroporous polymers and nanocomposites by spin-coating, J. Am. Chem. Soc. 126 (42) (2004) 13778–13786.

[3] S. KrishnaáKaruturi, L. TatáSu, T. KueiáChan, A.I. Tok, Gradient inverse opal photonic crystals via spatially controlled template replication of self-assembled opals, J. Nanoscale 3 (12) (2011) 4951–4954.

[4] G. Liu, L. Zhou, Y. Wu, C. Wang, Q. Fan, J. Shao, The fabrication of full color P (S t-MAA) photonic crystal structure on polyester fabrics by vertical deposition self-assembly, J. Appl. Polym. Sci. 132 (2015) 13.

[5] J.-M. Meijer, F. Hagemans, L. Rossi, D.V. Byelov, S.I. Castillo, A. Snigirev, I. Snigireva, A.P. Philipse, A.V. Petukhov, Self-assembly of colloidal cubes via vertical deposition, Langmuir 28 (20) (2012) 7631–7638.

[6] J. Shao, Y. Zhang, G. Fu, L. Zhou, Q. Fan, Preparation of monodispersed polystyrene microspheres and self-assembly of photonic crystals for structural colors on polyester fabrics, J. Text. Inst. 105 (9) (2014) 938–943.

[7] Z. Zhou, X. Zhao, Opal and inverse opal fabricated with a flow-controlled vertical deposition method, Langmuir 21 (10) (2005) 4717–4723.

[8] Z. Cai, Y.J. Liu, J. Teng, X.J.A.a.m. Lu, Fabrication of large domain crack-free colloidal crystal heterostructures with superposition bandgaps using hydrophobic polystyrene spheres, ACS Appl. Mater. Interf. 4 (10) (2012) 5562–5569.

[9] M. Curti, J. Schneider, D.W. Bahnemann, C.B. Mendive, Inverse opal photonic crystals as a strategy to improve photocatalysis: underexplored questions, J. Phys. Chem. Lett. 6 (19) (2015) 3903–3910.

[10] P. Jiang, G.N. Ostojic, R. Narat, D.M. Mittleman, V.L. Colvin, The fabrication and bandgap engineering of photonic multilayers, Adv. Mater. 13 (6) (2001) 389–393.

[11] Q. Yan, L.K. Teh, Q. Shao, C. Wong, Y.-M. Chiang, Layer transfer approach to opaline hetero photonic crystals, Langmuir 24 (5) (2008) 1796–1800.

[12] Dusseault, T. J.; Gires, J.; Barako, M. T.; Won, Y.; Agonafer, D. D.; Asheghi, M.; Santiago, J. G.; Goodson, K. E. In Inverse opals for fluid delivery in electronics cooling systems, 2014 IEEE Intersociety Conference on Thermal and Thermomechanical Phenomena in Electronic Systems (ITherm), IEEE: 2014; pp 750-755.

[13] Q. Pham, M. Barako, J. Tice, Y. Won, Microscale Liquid Transport in Polycrystalline Inverse Opals across Grain Boundaries, Sci. Rep. 7 (1) (2017) 10465.

[14] R. Ranjan, J.Y. Murthy, S.V. Garimella, U. Vadakkan, M. Transfer, A numerical model for transport in flat heat pipes considering wick microstructure effects, Int. J. Heat Mass Transf. 54 (1–3) (2011) 153–168.

[15] R. Ranjan, J.Y. Murthy, S.V. Garimella, Analysis of the wicking and thin-film evaporation characteristics of microstructures, J. Heat Transfer 131 (10) (2009) 101001.

[16] Zhang, C.; Rong, G.; Palko, J. W.; Dusseault, T. J.; Asheghi, M.; Santiago, J. G.; Goodson, K. E., IPACK2015-48262.

[17] N.A. Kotov, Y. Liu, S. Wang, C. Cumming, M. Eghtedari, G. Vargas, M. Motamedi, J. Nichols, J. Cortiella, Inverted colloidal crystals as three-dimensional cell scaffolds, Langmuir 20 (19) (2004) 7887–7892.

[18] J. Lee, S. Shanbhag, N.A.J.J.o.M.C. Kotov, Inverted colloidal crystals as three-dimensional microenvironments for cellular co-cultures, J. Mater. Chem. 16 (35) (2006) 3558–3564.

[19] K.Y. Lee, J. Chun, J.H. Lee, K.N. Kim, N.R. Kang, J.Y. Kim, M.H. Kim, K.S. Shin, M.K. Gupta, J.M. Baik, Hydrophobic sponge structure-based triboelectric nanogenerator, Adv. Mater. 26 (29) (2014) 5037–5042.

[20] Y. Zhang, S. Wang, M. Eghtedari, M. Motamedi, N.A. Kotov, Inverted-colloidal-crystal hydrogel matrices as three-dimensional cell scaffolds, Adv. Funct. Mater. 15 (5) (2005) 725–731.

[21] H. Fudouzi, Fabricating high-quality opal films with uniform structure over a large area, J. Colloid Interf. Sci. 275 (1) (2004) 277–283.

[22] S. Wong, V. Kitaev, G.A. Ozin, Colloidal crystal films: Advances in universality and perfection, J. Am. Chem. Soc. 125 (50) (2003) 15589–15598.

[23] L. Teh, N. Tan, C. Wong, S. Li, Growth imperfections in three-dimensional colloidal self-assembly, J. Appl. Phys. A 81 (7) (2005) 1399–1404.

[24] G. Liu, Z. Wang, Y. Ji, Influence of growth parameters on the fabrication of high-quality colloidal crystals via a controlled evaporation self-assembly method, Thin Solid Films 518 (18) (2010) 5083–5090.

[25] Y.-H. Ye, F. LeBlanc, A. Haché, V.-V. Truong, Self-assembling three-dimensional colloidal photonic crystal structure with high crystalline quality, J. Appl. Phys. Lett. 78 (1) (2001) 52–54.

[26] Z.Y. Cai, J.H. Teng, Y. Wan, X.S. Zhao, An improved convective self-assembly method for the fabrication of binary colloidal crystals and inverse structures, J. Colloid Interf. Sci. 380 (2012) 42–50.

[27] L.B. Zhang, Y.Y. Xiong, Rapid self-assembly of submicrospheres at liquid surface by controlling evaporation and its mechanism, J. Colloid Interf. Sci. 306 (2) (2007) 428–432.

[28] Chiu, R. C.; Cima, M. J. J. J. o. t. A. C. S., Drying of granular ceramic films: II, drying stress and saturation uniformity. J Am Ceran Soc 1993, 76 (11), 2769-2777.

[29] R.C. Chiu, T. Garino, M. Cima, Drying of granular ceramic films: I, effect of processing variables on cracking behavior, J. Am. Ceram. Soc. 76 (9) (1993) 2257–2264.

[30] K.B. Singh, L.R. Bhosale, M.S. Tirumkudulu, Cracking in drying colloidal films of flocculated dispersions, Langmuir 25 (8) (2009) 4284–4287.

[31] H.N. Yow, M. Goikoetxea, L. Goehring, A.F. Routh, Effect of film thickness and particle size on cracking stresses in drying latex films, J. Colloid Interf. Sci. 352 (2) (2010) 542–548.

[32] B. Hatton, L. Mishchenko, S. Davis, K.H. Sandhage, J. Aizenberg, Assembly of large-area, highly ordered, crack-free inverse opal films, Proc. Natl. Acad. Sci. U S A 107 (23) (2010) 10354–10359.

[33] L.K. Wang, X.S. Zhao, Fabrication of crack-free colloidal crystals using a modified vertical deposition method, J. Phys. Chem. C 111 (24) (2007) 8538–8542.

[34] Y. Suh, Q. Pham, B.W. Shao, Y. Won, The control of colloidal grain boundaries through evaporative vertical self-assembly, Small 15 (2019) 12.

[35] B. Li, B.B. Jiang, W. Han, M. He, X. Li, W. Wang, S.W. Hong, M. Byun, S.L. Lin, Z.Q. Lin, Harnessing colloidal crack formation by flow-enabled self-assembly, Angew. Chem. Int. Ed. 56 (16) (2017) 4554–4559.

[36] D. Coursault, J. Grand, B. Zappone, H. Ayeb, G. Levi, N. Felidj, E. Lacaze, Linear self-assembly of nanoparticles within liquid crystal defect arrays, Adv. Mater. 24 (11) (2012) 1461–1465.

[37] B.-H. Wu, C. Zhang, N. Zheng, L.-W. Wu, Z.-K. Xu, L.-S. Wan, Grain Boundaries of self-assembled porous polymer films for unclonable anti-counterfeiting, ACS Appl. Polym. Mater. 1 (1) (2018) 47–53.

[38] M. Gultekinoglu, X.Y. Jiang, C. Bayram, H. Wu, K. Ulubayram, M. Edirisinghe, Self-assembled micro-stripe patterning of sessile polymeric nanofluid droplets, J Colloid Interf Sci 561 (2020) 470–480.

[39] M.F. Zhao, W. Luo, X. Yong, Harnessing complex fluid interfaces to control colloidal assembly and deposition, J. Colloid Interf. Sci. 540 (2019) 602–611.

[40] N.V. Dziomkina, M.A. Hempenius, G.J. Vancso, Towards true 3-dimensional BCC colloidal crystals with controlled lattice orientation, Polymer 50 (24) (2009) 5713–5719.

[41] L. Woodcock, Entropy difference between the face-centred cubic and hexagonal close-packed crystal structures, Nature 385 (6612) (1997) 141.

[42] I. Lokteva, M. Koof, M. Walther, G. Grubel, F. Lehmkuhler, Monitoring nanocrystal self-assembly in real time using in situ small-angle X-Ray scattering, Small 15 (20) (2019) e1900438.

[43] M.C. Weidman, D.M. Smilgies, W.A. Tisdale, Kinetics of the self-assembly of nanocrystal superlattices measured by real-time in situ X-ray scattering, Nat. Mater. 15 (7) (2016). 775-+.

[44] V.N. Manoharan, Colloidal matter: packing, geometry, and entropy, Science 349 (2015) 6251.

[45] J. Bahadur, D. Sen, S. Mazumder, B. Paul, A. Khan, G. Ghosh, Evaporation-induced self assembly of nanoparticles in non-buckling regime: Volume fraction dependent packing, J. Colloid Interf. Sci. 351 (2) (2010) 357–364.

[46] F.F. Shao, T.W. Ng, J. Efthimiadis, A. Somers, W. Schwalb, Evaporative micro-particle self assembly influenced by capillary evacuation, J. Colloid Interf. Sci. 377 (2012) 421–429.

[47] H. Rochlitz, P. Scholz, Application of laser-induced fluorescence technique in a duct flow with one heated wall, Exp. Fluids 59 (2018) 3.

[48] W. Chaze, O. Caballina, G. Castanet, F. Lemoine, Spatially and temporally resolved measurements of the temperature inside droplets impinging on a hot solid surface, Exp. Fluids 58 (2017) 8.

[49] R.S. Volkov, P.A. Strizhak, Planar laser-induced fluorescence diagnostics of water droplets heating and evaporation at high-temperature, Appl. Therm. Eng. 127 (2017) 141–156.

[50] J. Feng, L. Xiong, S.Q. Wang, S.Y. Li, Y. Li, G.Q. Yang, Fluorescent temperature sensing using triarylboron compounds and microcapsules for detection of a wide temperature range on the micro- and macroscale, Adv. Funct. Mater. 23 (3) (2013) 340–345.

[51] P. Low, B. Kim, N. Takama, C. Bergaud, High-spatial-resolution surface-temperature mapping using fluorescent thermometry, Small 4 (7) (2008) 908–914.

[52] D. Erickson, D. Sinton, D.Q. Li, Joule heating and heat transfer in poly (dimethylsiloxane) microfluidic systems, Lab Chip 3 (3) (2003) 141–149.

[53] R. Samy, T. Glawdel, C.L. Ren, Method for microfluidic whole-chip temperature measurement using thin-film poly(dimethylsiloxane)/Rhodamine B, Anal. Chem. 80 (2) (2008) 369–375.

[54] T. Glawdel, Z. Almutairi, S. Wang, C. Ren, Photobleaching absorbed Rhodamine B to improve temperature measurements in PDMS microchannels, Lab Chip 9 (1) (2009) 171–174.

[55] D. Ross, M. Gaitan, L.E. Locascio, Temperature measurement in microfluidic systems using a temperature-dependent fluorescent dye, Anal. Chem. 73 (17) (2001) 4117–4123.

[56] F. Vetrone, R. Naccache, A. Zamarron, A.J. de la Fuente, F. Sanz-Rodriguez, L.M. Maestro, E.M. Rodriguez, D. Jaque, J.G. Sole, J.A. Capobianco, Temperature sensing using fluorescent nanothermometers, ACS Nano 4 (6) (2010) 3254–3258.

[57] J. Feng, K.J. Tian, D.H. Hu, S.Q. Wang, S.Y. Li, Y. Zeng, Y. Li, G.Q. Yang, A triarylboron-based fluorescent thermometer: sensitive over a wide temperature range, Angew. Chem. Int. Ed. 50 (35) (2011) 8072–8076.

[58] Suh, Y.; Lin, C.-H.; Gowda, H.; Won, Y. In Evaporation Rate Measurement at Multiple Scales Using Temperature-Sensitive Fluorescence Dyes, ASME 2019 International Technical Conference and Exhibition on Packaging and Integration of Electronic and Photonic Microsystems, American Society of Mechanical Engineers Digital Collection.

[59] H.F. Arata, P. Low, K. Ishizuka, C. Bergaud, B. Kim, H. Noji, H. Fujita, Temperature distribution measurement on microfabricated thermodevice for single biomolecular observation using fluorescent dye, Sens. Actuat. B-Chem. 117 (2) (2006) 339–345.

[60] T. Behnke, C. Wurth, E.M. Laux, K. Hoffmann, U. Resch-Genger, Simple strategies towards bright polymer particles via one-step staining procedures, Dyes Pigm. 94 (2) (2012) 247–257.

[61] J.H. Lee, I.J. Gomez, V.B. Sitterle, J.C. Meredith, Dye-labeled polystyrene latex microspheres prepared via a combined swelling-diffusion technique, J. Colloid Interface Sci. 363 (1) (2011) 137–144.

[62] A. Reisch, A.S. Klymchenko, Fluorescent Polymer Nanoparticles Based on Dyes: Seeking Brighter Tools for Bioimaging, Small 12 (15) (2016) 1968–1992.

[63] D. Greszik, H. Yang, T. Dreier, C. Schulz, Measurement of water film thickness by laser-induced fluorescence and Raman imaging, Appl. Phys. B-Lasers Opt. 102 (1) (2011) 123–132.

[64] J.M. Murray, P.L. Appleton, J.R. Swedlow, J.C. Waters, Evaluating performance in three-dimensional fluorescence microscopy, J. Microsc. 228 (3) (2007) 390–405.

[65] J.R. Swedlow, K. Hu, P.D. Andrews, D.S. Roos, J.M. Murray, Measuring tubulin content in Toxoplasma gondii: a comparison of laser-scanning confocal and wide-field fluorescence microscopy, Proc. Natl. Acad. Sci. 99 (4) (2002) 2014–2019.

[66] J.C. Waters, Accuracy and precision in quantitative fluorescence microscopy, J. Cell Biol. 185 (7) (2009) 1135–1148.

[67] Youngjoon Suh, Cheng-Hui Lin, Hamsa Gowda, Yoonjin Won, Multiscale Evaporation Rate Measurement Using Microlaser-Induced Fluorescence, J. Electron. Packag. 142 (3) (2020), https://doi.org/10.1115/1.4046767. In this issue 031105.